Light-induced matter vortex transitions

P.J. Aguilera-Rojas [ID], M.G. Clerc [ID], M. Diaz-Zuniga [ID] *, R. Gajardo-Pizarro [ID]

Departamento de Física and Millennium Institute for Research in Optics, FCFM, Universidad de Chile, Casilla 487-3, Santiago, Chile

ARTICLE INFO

ABSTRACT

Optical vortices have attracted attention due to their intrinsic characteristics and potential applications, which span from telecommunication in free space and image analysis to manipulating small particles. Optical valves and liquid crystal cells have been fundamental in generating optical vortex beams. The theoretical description predicts the existence of different Rayleigh and standard vortices. Based on two different experiments, we investigate the transition between these vortices. When the effect of topological forcing is dominant, the bifurcation diagram between these vortices has been characterized through both experimental and numerical means. The numerical and experimental findings present qualitative agreement.

1. Introduction

Optical vortices (OAM) are beams of light that have point phase dislocations around which the electromagnetic field usually has a spiral structure; that is, these dislocations are singular points where the electromagnetic field cancels out and around which the phase distribution forms a spiral with N arms, where N is the topological charge [1–3]. In the last decade, optical vortices have attracted attention for their diverse photonic applications [4], ranging from angular momentum exchange between light and matter [5], optical tweezers [6–8], quantum computing [9], astronomical image enhancement [10], optical beam generation by micro/nano-patterning in liquid crystals [11,12], and data transmission [13]. Several methods have been proposed to generate vortices, such as spiral phase plates [14], diffractive elements [15,16], liquid crystal cells with radial director orientation, *q-plates* [17], liquid crystal droplets [18], liquid crystals cells with umbilical defects [19] with magnet and oscillatory electric field [20,21] or liquid crystal light valves [22–24]. In the case of optical valves, the emergence of vortex beams is related to the fact that the Gaussian incident beam on the photoconductor layer induces an inhomogeneous voltage with a hedgehog-type shape, which causes an umbilic vortex in the liquid crystal, which then interacts with the light, generating a vortex beam. This umbilical defect is taken into account by considering the system close to the reorientation instability of the liquid crystal molecules, which is described by the Ginzburg–Landau equation at real coefficients and with topological forcing [24]. The umbilical defect can be located in the center of the beam (see Fig. 1) or far from it, depending on the balance between forcing and spatial inhomogeneities. In the latter case, the defect is referred to as a shadow vortex [25], as its topological charge is in the unilluminated area. Likewise, the amplitude

equation predicts analytically that when the bifurcation parameter is below and away from the critical reorientation point of the liquid crystal molecules; the system presents a vortex of small amplitude with a large core, called the Rayleigh vortex [26], due to its shape (cf. Fig. 1). Experimental observation of these vortices and the transition between them and standard ones has yet to be established.

The letter aims to gain a deeper understanding of the formation and transition of Rayleigh vortices to standard ones through an experimental approach. Two experiments were conducted to observe the formation of Rayleigh and standard vortices, as well as their transitions: (i) in a liquid crystal light valve (LCLV) with homeotropic anchoring and transmission configuration and (ii) in a nematic liquid crystal cell (NLCC) with homeotropic anchoring under the effect of a magnetic ring and oscillating electric field. The bifurcation diagram between these vortices has been characterized experimentally and numerically when the effect of topological forcing is dominant. The numerical and experimental findings present qualitative agreement.

2. Experimental liquid crystal light valve setup

We will consider two experimental configurations to study the transition between vortices. A liquid crystal light valve in transmission and liquid crystal cells under the combined effect of a magnet ring and oscillatory electric field.

The experimental setup for vortex induction by light is schematically illustrated in Fig. 1. The LCLV, provided by HoloEye, is composed of a nematic liquid crystal layer (MLC 6608 Merck) deposited between two parallel glass plates separated by a distance d = 15 μm. The
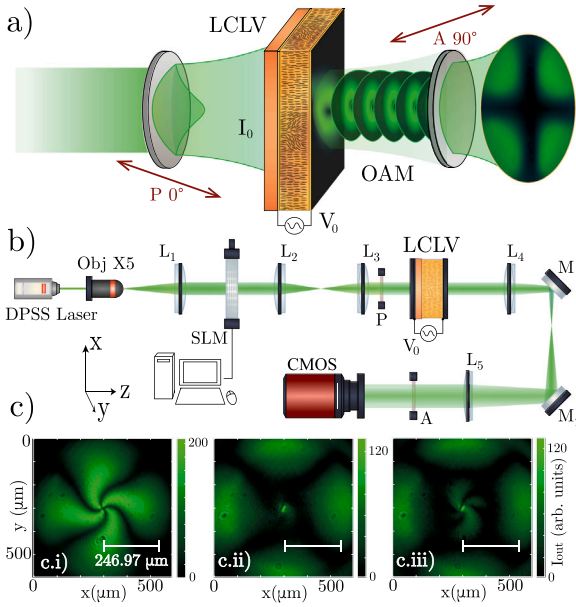

Fig. 1. Experimental vortex setup in Liquid Crystal Light Valve (LCLV). (a) Schematic illustration of matter vortex inducing OAM light modes. The right green beam accounts for the incident Gaussian light. (b) Schematic representation of experimental setup, where DPSS is a diode-pumped solid-state laser, L and M account for the lenses and mirrors considered, SLM is a spatial light modulator, P and A are the cross polarizers, V_0 is the driven voltage, I_0 is the light intensity applied to LCLV, Obj stands for a microscope objective with a magnification of $\times 5$, and CMOS is a complementary metal–oxide–semiconductor camera. (c) Snapshots of experimental-type vortex solutions: (c.i) Standard, (c.ii) Rayleigh, and (c.iii) Rayleigh-standard vortex transition.

plates feature transparent conductive indium tin oxide (ITO) films and a transparent photoconductive slab, $Bi_{12}SiO_{20}$ (BSO), with dimensions of 25×25 mm^2 and a thickness of 1 mm. The interior surfaces are treated to obtain a homeotropic anchoring for the liquid crystal, such that the nematic director is orthogonal to the confinement walls. The liquid crystal has a negative dielectric anisotropy $\epsilon_a = \epsilon_\parallel - \epsilon_\perp = -4.2\epsilon_o$, with $\epsilon_\parallel$ and $\epsilon_\perp$ the dielectric susceptibility for the electric fields parallel and orthogonal, respectively. An oscillatory voltage V_0 rms can be applied to the LCLV through the ITO films at a frequency $f_0 = 1.0$ kHz. Furthermore, when a light beam is incident upon the BSO wall of the LCLV due to the photo-generated charges, an extra non-homogeneous bias, in function of the light beam profile, is applied. This bias can be modeled as $V_I = \alpha I(r)$ for a Gaussian light beam of small intensity [24]. This induced an effective bias $V_{eff} = V_0 + \alpha I(r)$, where r and θ are the transverse coordinates that describe the liquid crystal sample. Namely, the voltage applied to the nematic liquid crystal sample has two parts: one spatially homogeneous V_0, externally imposed, and another inhomogeneous $\alpha I(r)$, Gaussian-shaped part imposed by the illumination. Note that the voltage is invariant under rotations in the plane orthogonal to the illumination. When the effective bias $V_{eff}(r)$ is locally above the voltage of Fréedericksz transition V_{FT}, that means $V_{eff}(r) - V_{FT} > 0$ for a specific spatial local region, a molecular reorientation occurs, following the intensity gradients associated with the Gaussian beam profile. This induces a localized matter vortex on the liquid crystal [22–24]. For the experimental realization of localized induction, a diode-pumped solid-state laser, $\lambda_0 = 532$ nm, with TEM 00 light mode is employed. The beam is expanded by a microscope objective with a magnification of $\times 5$. To control the beam shape, a spatial light modulator (SLM, LC 2012 Spatial Light Modulator Holoeye, transmission) is considered This SLM is based on a twisted nematic liquid crystal display, which generates a simple phase modulation and a coupled polarization effect, resulting likewise in amplitude modulation. The light beam is transmitted through the LCLV and is amplified $\times 3$ approximately by a free-space telescope system to observe the vortex

generated by the light. The LCLV is placed between two crossed linear polarizers, and the product of the polarization reorientation produced by the matter vortex is observed. The vortex induction is monitored by a complementary metal–oxide–semiconductor (CMOS) camera.

For voltages V_0 below the Fréedericksz transition and with sufficiently large light intensity, one observes the generation of standard vortices [see Fig. 1(c).i]. These standard vortices are characterized by centering their position at the center of the light beam. The director $\vec{n}$ shows a significant reorientation around the vortex position in a region of the order of the square root of the elastic constants of nematic liquid crystals [27]. This region of the vortex is usually called a *vortex core*. Hence, if no light is applied and the voltage exceeds the critical reorientation voltage, the same vortices are observed on the liquid crystal sample.

3. Theoretical description for localized vortex induction

The dynamics of nematic liquid crystals is driven by minimizing the Frank–Oseen free energy $\mathcal{F}$ when thermal variations are neglected. The Frank–Oseen free energy has the form [28,29]

$$\mathcal{F}[\vec{n}] = \int \left(\frac{K_1(\vec{\nabla} \cdot \vec{n})^2}{2} + \frac{K_2(\vec{n} \cdot \vec{\nabla} \times \vec{n})^2}{2} \right) dV$$
$$+ \int \left(\frac{K_3(\vec{n} \times \vec{\nabla} \times \vec{n})^2}{2} + \frac{\epsilon_a(\vec{E} \cdot \vec{n})}{2} \right) dV, \quad (1)$$

where $\{K_1, K_2, K_3\}$ are, respectively, the splay, twist, and bend elastic constants of the nematic liquid crystal, V accounts for the volume of the liquid crystal sample, ϵ_a is the anisotropic dielectric constant, and $\vec{E}$ is the electric field applied to the sample. The director only considers the molecule's average orientation, so one considers constraint $\|\vec{n}\|^2 = 1$. To describe the dynamics of the illuminated liquid-crystal light valve, filled with a negative dielectric anisotropic nematic liquid crystal ($\epsilon_a < 0$), homeotropic anchoring, and consider the normalization constrain of the director, the dynamics of the molecular director $\vec{n}$, reads

$$\gamma \frac{d\vec{n}}{dt} = -\frac{\partial \mathcal{F}}{\partial \vec{n}} - \vec{n} \left(\frac{\partial \mathcal{F}}{\partial \vec{n}} \cdot \vec{n} \right) = K_3 \left[\nabla^2 \vec{n} - \vec{n} \left(\vec{n} \cdot \nabla^2 \vec{n} \right) \right]$$
$$+ (K_3 - K_1) \left[\vec{n}(\vec{n} \cdot \vec{\nabla})(\vec{\nabla} \cdot \vec{n}) - \vec{\nabla}(\vec{\nabla} \cdot \vec{n}) \right]$$
$$+ (K_2 - K_3) \left\{ 2(\vec{n} \cdot (\vec{\nabla} \times \vec{n}))(\vec{n}(\vec{n} \cdot (\vec{\nabla} \times \vec{n})) - (\vec{\nabla} \times \vec{n})) \right.$$
$$\left. + \vec{n} \times \left[\vec{\nabla} \left(\vec{n} \cdot (\vec{\nabla} \times \vec{n}) \right) \right] \right\} - \epsilon_a(\vec{n} \cdot \vec{E}) \left[(\vec{n} \cdot \vec{E})\vec{n} - \vec{E} \right], \quad (2)$$

where γ is the torque relaxation time. The sample can be considered to consist of two parallel flat plates separated by a thickness d that applied an effective voltage drop $V_{eff}(r)$ composed by a homogeneous voltage V_0 and inhomogeneous voltage $\alpha I(r)$ as a consequence of the illumination of the optical valve. The electric field inside the sample has the form

$$\vec{E} = E_z\hat{z} + E_r\hat{r} = -\vec{\nabla}V_{eff} = -\frac{1}{d}(V_0 + \alpha I(r))\hat{z} - \frac{z\alpha}{d}\frac{dI(r)}{dr}\hat{r}. \quad (3)$$

3.1. Weakly nonlinear analysis

A trivial solution of Eq. (2) when the photoconductor effect is neglected is the homeotropic state $\vec{n} = \hat{z}$. Under crossed polarizers, this state corresponds to a completely dark state in the microscope. The homeotropic state undergoes a stationary instability for critical values of the voltage that match with the Fréedericksz transition threshold $V_{FT} = \sqrt{-K_3\pi^2/\epsilon_a}$. To figure out the director dynamics close to the re-orientational instability, we can consider the approach of a weakly nonlinear analysis and the effects of the inhomogeneous field as perturbative. Let us introduce the Ansatz

$$\vec{n} = \begin{pmatrix} X(\vec{r}'_\perp, t)\sin\left(\frac{\pi z}{d}\right) \\ Y(\vec{r}'_\perp, t)\sin\left(\frac{\pi z}{d}\right) \\ 1 - \frac{(X^2+Y^2)}{2}\sin^2\left(\frac{\pi z}{d}\right) \end{pmatrix} + \vec{W}(X, Y), \quad (4)$$

where $\vec{r}'_\perp = (x, y)$ is the transverse coordinate and $\vec{W}(X, Y)$ accounts for the small nolinear corrections. Considering the Ansatz (4) in Eq. (2), close to the re-orientational instability, $V_0 \sim V_{FT}$, introducing the complex field $A(\vec{r}, t) \equiv (X + iY)/\sqrt{[(d/\pi)^2(2K_1 - K_3) - 3\epsilon_a E_z^2]/4}$, scaling the space and time as $\vec{r} = \vec{r}'_\perp/\sqrt{2/(K_1 + K_2)}$ and $t = \tau/\gamma$, linearized in $\vec{W}(X, Y)$, and imposed the solvability conditions after straightforward calculations, we get (the Ginzburg–Landau-like amplitude equation, for more details, see Ref. [24,30])

$$\partial_\tau A = \mu(r)A - |A|^2 A + \nabla^2 A + \delta \partial_{\eta\eta}\bar{A} + f(r)e^{i\theta}, \qquad (5)$$

where the amplitude A accounts for the projection of the director on the plane of the liquid crystal sample, and $\bar{A}$ is the complex conjugate of A. $\partial_\eta = \partial_x + i\partial_y$ is the Wirtinger derivative, $\nabla^2 = \partial_{\eta\bar{\eta}}$ stands for the Laplacian operator, $\{r, \theta\}$ are the cylindrical coordinates that describe the transversal direction of the sample. $\delta \equiv (K_1 - K_2)/(K_1 + K_2)$ accounts for the different elastic constants of the liquid crystal. $\mu \approx \mu_0 + \mu_1(r)$ is the bifurcation parameter where $\mu_0 = -K_3 k^2 - \epsilon_a V_0^2/d^2$ and $\mu_1(r) = \epsilon_a 2\alpha V_0 I(r)/d^2$. Indeed, the bifurcation parameter is formed by a constant μ_0 that accounts for the elastic and driven voltage balance, plus a spatial Gaussian voltage proportional to the light intensity $I(r) = e^{-r^2/2\omega^2}$, and the topological forcing $f(r) \equiv \epsilon_a 2d E_r(r)E_z(r)/z\pi$ is a consequence of the radial component of the electric field inside the liquid crystal sample and proportional to spatial variation of the light beam $dI(r)/dr = -(r/\omega)e^{-r^2/2\omega^2}$, the Rayleigh function. Note that a similar amplitude equation with complex coefficients has been derived for a resonant optical cavity-filled with a nonlinear medium and pumping with an orbital angular momentum beam [31]. Eq. (5) provides a quantitative and quantitative description of the LCLV system close to re-orientational instability, Fréedericksz transition. Far from this transmission, Eq. (5) only qualitatively describes the observed dynamics.

Note that the Ginzburg–Landau equation [Eq. (5) with $\delta = 0$ and $f = 0$] is an equation that is invariant under phase symmetry ($A \rightarrow Ae^{i\phi_0}$) and coordinate rotation transformations ($\partial_\eta \rightarrow e^{i\phi_1}\partial_\eta$). However, since Ginzburg–Landau-like Eq. (5) considers different elastic deformations of liquid crystals ($K_1 \neq K_2 \neq K_3$), which are determined by the director's orientation, the aforementioned symmetries are not satisfied separately. Hence, this model Eq. (5) is not an invariant by a single rotation. Instead, Eq. (6) is invariant under simultaneous symmetry phase and rotation $A \rightarrow Ae^{i\phi_0}$ and $\partial_\eta \rightarrow e^{i\phi_0}\partial_\eta$ [27].

Numerical simulations of the amplitude Eq. (2) for a positive bifurcation parameter show vortices similar to those of the Ginzburg–Landau equation, the standard vortex [24]. Observe that analytical expressions for these vortices are unknown. Likewise, vortices of small amplitude and large radius are presented for negative bifurcation parameters due to topological forcing, Rayleigh vortex [26]. These last vortices have analytical expressions.

3.2. Rayleigh vortex

To study the vortices when the bifurcation parameter is negative $\mu(r) < 0$, we consider the following scaling of the spatial variable $\rho = r/\omega$, where ω is the beam waist, the amplitude Eq. (5) is rewritten as

$$0 = \mu(\rho)A - |A|^2 A + \frac{1}{\omega^2}\nabla^2 A + \frac{\delta}{\omega^2}\partial_{\eta\eta}\bar{A} + f(\rho)e^{i\theta}. \qquad (6)$$

Considering the limit of wide and weak light beam ($\omega \gg 1$ and $I(r) \ll 1$), the Thomas–Fermi-like approximation, on Eq. (6), we can neglect the spatial derivatives

$$0 \approx \mu(\rho)A - |A|^2 A + f(\rho)e^{i\theta}. \qquad (7)$$

Assuming a small amplitude ansatz, we neglected the cubic term on Eq. (7), resulting in the solution (Rayleigh vortex) [26]

$$A(r) \approx -\frac{1}{\mu_0}f(r)e^{i\theta} \propto \left(\frac{r}{\omega}\right)e^{-r^2/2\omega^2}e^{i\theta}. \qquad (8)$$
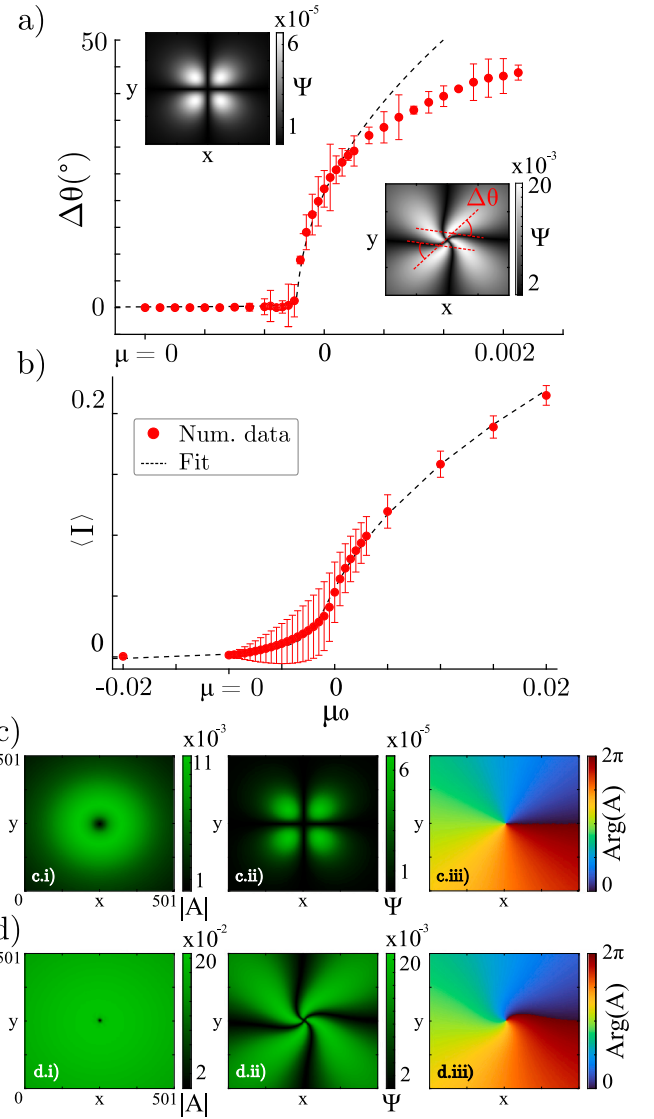

Fig. 2. Numerical bifurcation diagrams of the vortex transition for the amplitude Eq. (5) for $\mu_1 = 0.019$, $\delta = 0.2$, $f(r) = 0.008(r/\omega^2)e^{-r^2/2\omega^2}$, $\omega = 100$. (a) Variation of the angle of the nullclines $\Delta\theta$ with respect to the horizontal direction as a function of the homogeneous bifurcation parameter μ_0. The red dots and their respective error bars are the error bars come from two sweeps of numerical simulations of the amplitude Eq. (5) and also take the standard deviation considering the angles obtained from the different arms of the vortex. The dashed curve accounts for the deterministic bifurcation curve, corresponding to a square root law. The insets account for the vortices observed in $\mu_0 = -0.01$ (left) and $\mu_0 = 0.001$ (right). (b) The total magnitude of the amplitude $\langle I \rangle = \iint |A(x, y)|^2 dxdy$ as a function of μ_0. The red dots and their respective error bars are obtained from numerical simulations. The dashed curve stands for the noisy bifurcation curve $\langle I \rangle = C_1\sqrt{(\mu_0 - \mu_c) + \sqrt{(\mu_0 - \mu_c)^2 + \eta_1}}$, for more details see Section 6 and formula (11), with $C_1 = 8.827$, $\mu_c = 0.9951$ and $\eta_1 = 0.00000001$ for the fit of (a), and $C_1 = 1.099$, $\mu_c = 0.9985$ and $\eta_1 = 0.5555517$ for (b). (c) Rayleigh Vortex: stationary solution of Eq. (5) for $\mu_0 = -0.01$, (c.i) amplitude field $|A|$, (c.ii) polarization field Ψ, (c.iii) phase field of complex amplitude $Arg(A)$. (d) Standard Vortex: stationary solution of Eq. (5) for $\mu_0 = 0.001$, (d.i) amplitude field $|A|$, (d.ii) polarization field Ψ, (d.iii) phase field of complex amplitude $Arg(A)$.

This vortex is characterized by growing radially linearly around the phase singularity and, far from it, decaying in a Gaussian manner. Due to the above property, the vortex (8) is called the Rayleigh vortex. Note that this solution is supported by the topological forcing, whose shape and size are given by the light intensity profile. Fig. 2c shows a Rayleigh vortex obtained numerically from Eq. (5). In the case of a resonant optical cavity filled with a nonlinear medium and pumping

with an orbital angular momentum beam similar Rayleigh vortex was obtained [31]. However, one expects that the dynamics and instabilities of this solution are different from those that we observe due to the complex coefficients included in the model that describes the nonlinear cavity,

3.3. Standard vortex

The Ginzburg–Landau equation at real coefficients in two dimensions, similar to Eq. (5), predicts the emergence of vortex solutions when $\mu > 0$. In the nematic liquid crystal, these vortex solutions are usually denominated as a standard vortex. These vortices are characterized by singularity phase points where the amplitude A vanishes. The phase acquires a spiral twist in space near this singular point due to the medium elastic anisotropy [24]. The δ parameter characterizes this anisotropy. The phase torsion allows us to observe these vortices in the polarization space as a swastika/svastika-type texture (cf. Fig. 2d), depending on the elastic constants of the media and the initial conditions [24]. Numerical and experimental evidence shows that a standard vortex can be induced and localized at the center of a Gaussian light beam [24]. These vortex solutions do not have an analytical expression for the Eq. (5). Fig. 2d depicts a standard vortex solution.

In contrast to a Rayleigh vortex, a standard vortex has a small core with a torsion in the phase near the core. The Rayleigh vortex solution has a larger core size proportional to the size of the Gaussian beam waist, as indicated in the approximate solution (8). These solutions are found in different regions of the μ parameter, and it is possible to characterize their transition as shown in Fig. 2c.

4. Numerical simulations

The study of the vortex transitions of Eq. (5) from an analytical point of view is a thorny task because there are no analytical solutions for the standard vortices. Numerical simulations of Eq. (5) are a logical approach to understanding this transition. Numerical simulations of Eq. (5) were implemented using a triangular finite element code with adaptive spatial and temporal steps based on the second-order implicit backward method was used, and a simulation box of dimensions 501×501 was considered.

In numerical simulations of the amplitude Eq. (5) for $\mu > 0$, a standard vortex is observed at the center of the Gaussian. The right inset of Figs. 2 shows a standard vortex. By decreasing μ_0 below the re-orientation instability, it is observed that the standard vortices must be replaced by vortices of minimum amplitude and with a nucleus of the order of the waist of the light beam, *the Rayleigh vortex*. Likewise, these vortices are characterized by having a Maltese cross in the polarization field $\psi = Re(A)Im(A)$ (cf. Fig. 2). One can characterize this transition by measuring the orientation of the nullclines $\Delta\theta$ for the horizontal orientation. Nullclines correspond when the real or imaginary part of the amplitude is zero. Fig. 2a summarizes the variation of $\Delta\theta$ as a function of μ_0. Note that $\Delta\theta$ follows a square root law. Likewise, when the total intensity of the amplitude $\langle I \rangle = \iint |A(x,y)|^2 dx\,dy$ is measured, the system presents a subcritical transition as illustrated in Fig. 2b.

To generate the bifurcation diagrams in Fig. 2, an increasing and decreasing sweep of the μ_0 parameter was performed, which accounts for the bifurcation point of the system. This was done starting with a zero solution initial condition and recording the solutions at each increase/decrease of μ_0. Thereafter, an average was estimated with its respective error bar. To calculate the angular torsion, we perform image processing of the polarization field to detect and interpolate the nullclines of each vortex. We then compare the inclination of these nullclines with respect to the Cartesian axis in their central and external zones, which are delimited by the maximum point of the derivative of the interpolated nullcline. This accounts for the maximum torsion of this. Subsequently, the mean value of the difference between the inclination angles of each zone is calculated, resulting in the angle of torsion
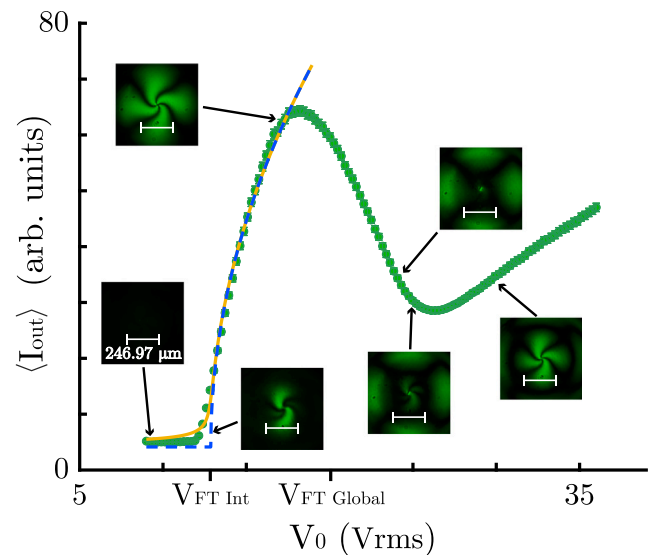

Fig. 3. Total intensity $\langle I_{\text{out}} \rangle$ as a function of the applied voltage V_0 to the LCLV. The green circles show the measured light intensity. The snapshots account for the vortices observed in the system with the applied voltage indicated by the arrows. The blue dashed and yellow curve account for a supercritical perfect and imperfect bifurcation obtained using the expression $\langle I_{\text{out}} \rangle = C_2 \sqrt{(V_0 - V_{\text{FT}}) + \sqrt{(V_0 - V_{\text{FT}})^2 + \eta_2}} + I_{\text{ref}}$, for more details see Section 6 and formula (11), with the common fitting parameters $C_2 = 19.937$ [arb.units/$\sqrt{V_{\text{rms}}}$], $V_{\text{FT}} = 12.8379\ V_{\text{rms}}$, and $I_{\text{ref}} = 3.4231$ [arb.units], and using $\eta_2 = 0$ [V_{rms}]^2 and $\eta_2 = 0.02701$ [V_{rms}]^2, respectively.

between the nullclines of each vortex and its different realizations during the sweep of μ_0, with the associated error bar.

Hence, the theoretical model Eq. (5) predicts that standard vortices must be replaced by vortices of minimal amplitude, with a core of the order of the waist of the light beam and cross structures, Rayleigh vortex. However, experimentally, this transition is challenging to discern, as light serves a dual function: on the one hand, it induces the vortex, and on the other, it illuminates the system to facilitate observation.

5. Experimental vortex transition

In experimental settings, when attempting to observe this vortex below the orientational transition, the system's darkness precludes the observation of the Rayleigh vortex. Fig. 3 illustrates the transition observed near the orientational transition. This chart shows the total intensity of the light as a function of the applied voltage to the LCLV. Note that optical valves exhibit oscillatory behavior for transmitting light when the applied voltage is changed [32,33]. Away from the orientational transition, the transmitted intensity declines, resulting in a reduction in the voltage induced by the light. This allows for the observation of the transition between standard and Rayleigh vortices. Thus, as the applied voltage increases, the vortex transformation is observed. It takes the shape of a cross, and its width is of the order of the illuminated area (see the insets of Figs. 1 and 3). For large voltages, we can see how a standard vortex emerges from the center of Rayleigh vortex (see the lowest inset of Fig. 3). All experimental observations in this setup were conducted at a temperature of 21° C.

6. Characterization of stochastic supercritical transition

A supercritical bifurcation is characterized by a continuous transition between two equilibria by moving the bifurcation parameter [34]. This type of bifurcation, in general, when described by an order parameter, is typically characterized by having a fixed value up to the bifurcation point, at which it begins to grow as the square root of the bifurcation parameter. The above bifurcation becomes imperfect
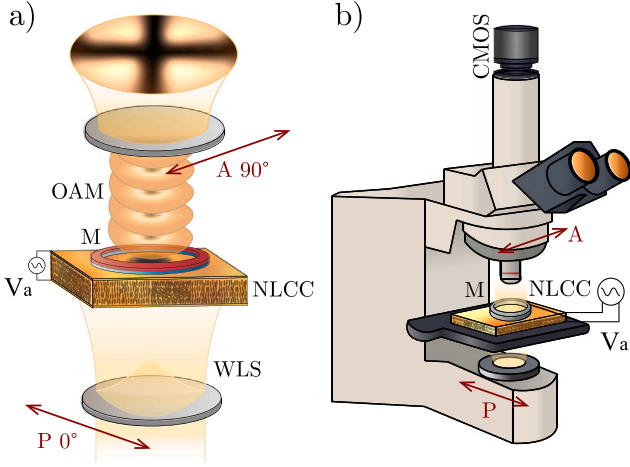
Fig. 4. Vortex transition in a nematic liquid crystal cell (NLCC) with homeotropic anchoring under the effect of a magnetic ring and oscillating electric field. (a) Illustration of the main elements of the experimental system. (b) Schematic representation of the experimental setup. NLCC is under the effect of a magnet ring (M) and an oscillatory electric field generated by a synodal-shape voltage $V = V_a \sin(\omega t)$, where V_a and ω are the amplitude and angular frequency of the applied voltage. P and A crossed and linear polarizers. A CMOS camera monitors the experiment. The sample is illuminated by a white light source (WLS).

when one considers the inherent fluctuations of macroscopic physical systems [35]. That is, below the bifurcation point, due to fluctuations, precursors of the equilibrium that is about to emerge are observed. The following amplitude equation describes a prototype model of this type of bifurcation

$$\partial_t C = \epsilon C - |C|^2 C + \sqrt{\kappa}\zeta(t), \qquad (9)$$

where $C(t)$ is a complex order parameter that describe the supercritical bifurcation, ϵ is the bifurcation parameter, κ is the noise intensity level and $\zeta(t)$ is a white noise, characterized by zero mean value $\langle\zeta\rangle = 0$ and correlation $\langle\zeta(t)\zeta(t')\rangle = \delta(t - t')$. In the case of the deterministic system, $\kappa = 0$, the module of the stable equilibrium is zero $C = 0$ ($C = \sqrt{\epsilon}$), when the bifurcation parameter is negative $\epsilon \leq 0$ (positive $\epsilon > 0$). From the Langevin Eq. (9), one can infer the Fokker–Planck equation when considering stochastic fluctuations. From this equation, one can find the stationary probability for the magnitude of amplitude, which satisfies [35]

$$P_s(|C|) = Q(\epsilon, \kappa)|C|e^{[\epsilon|C|^2 - |C|^4/2]/\kappa}, \qquad (10)$$

where $Q(\epsilon, \kappa) = 2\sqrt{2}e^{-\epsilon^2/2\kappa}/erfc(-\epsilon/\sqrt{2\kappa})\sqrt{\pi\kappa}$ is the normalization factor. The expectation value $\langle|C_{max}|\rangle$ of this distribution satisfies the simple expression [35]

$$\langle|C_{max}|\rangle = \sqrt{\frac{\epsilon + \sqrt{\epsilon^2 + \kappa}}{2}}, \qquad (11)$$

This statistic is very close to the mean value. However, the latter has a complex analytical expression. The formula (11) recovers the deterministic result in the weak noise limit. We have used the previous expression (11) to characterize experimentally the bifurcation point and the noise level intensity (cf. Figs. 2 and 3). It is worth noting that experimentally, the expression (11) allows us to determine quantitatively the values of the transition points for the control parameters $\epsilon = 0$, and quantify the total noise level intensity κ present in the system. Determining the bifurcation point in experimental systems is a complex problem when the inherent fluctuations are not negligible [35].

7. Liquid crystal cell under the effect of a magnetic ring

In order to examine the transition from a Rayleigh vortex to a standard vortex, we have conducted a further experiment based on a
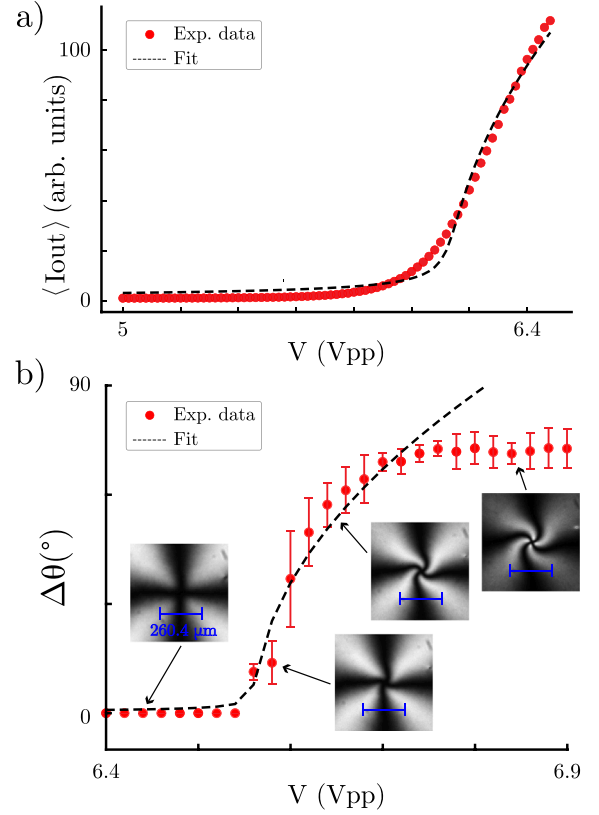

Fig. 5. Vortex transition characterization as a function of the voltage in a nematic liquid crystal cell with homeotropic anchoring under the effect of a magnetic ring and oscillating electric field. (a) Bifurcation diagram for total intensity $\langle I \rangle$ as a function of applied voltage V_0. The red circles are obtained experimentally. The dashed curve is obtained using the expression $\langle I_{out} \rangle = C_2 \sqrt{(V_0 - V_{FT}) + \sqrt{(V_0 - V_{FT})^2 + \eta_2}}$, for more details see Section 6 and formula (11), with the common fitting parameters $C_2 = 182.2$ [arb.units/$\sqrt{V_{rms}}$], $V_{FT} = 6.14$ V_{rms}, $\eta_2 = 0.0003$ [V_{rms}]^2. (b) Variation of the angle of the nullclines $\Delta\theta$ with respect to the horizontal direction as a function of the applied voltage V_0. The red circles and their respective error bars are obtained experimentally. The insets account for the vortices observed in the respective voltage emphasized with arrows. The dashed curve accounts for a supercritical transition using the expression $\langle I_{out} \rangle = C_2 \sqrt{(V_0 - V_{FT}) + \sqrt{(V_0 - V_{FT})^2 + \eta_2}}$, with the common fitting parameters $C_2 = 179.07796$ [°/$\sqrt{V_{rms}}$], $V_{FT} = 6.5602$ V_{rms}, $\eta_2 = 0.000004$ [V_{rms}]^2 for (b).

NLCC , with the addition of a magnetic ring and an oscillating field. Fig. 4 shows a schematic representation of the experimental setup. We consider a cell composed of two thin glass layers with transparent electrodes included (indium tin oxide with a thickness of 0.08 μm) and separated by a thickness of $d = 75$ μm, which are treated so that their inner walls have homogeneous homeotropic anchoring. By capillarity, the cell is filled with a nematic liquid crystal LC-BYVA-01 (INSTEC) with negative dielectric anisotropy $\epsilon_a = -4.8\epsilon_0$, rotation viscosity $\gamma = 204$ mPa·s, splay and bend elastic constants $K_1 = 17.65$ pN and $K_3 = 21.39$ pN, respectively, and negative magnetic anisotropy χ_a (not measured yet). A neodymium magnetic ring of 3200 G on the surface with a rectangular cross-section, outer radius $R_{out} = 7$ mm, inner radius $R_{in} = 2$ mm, and thickness $h = 5$ mm is placed on the top of NLCC. The sample is placed in the microscope (Olympus BX51), sandwiched between two crossed linear polarizers and illuminated with a white light (halogen lamp). A sinusoidal voltage $V(t)$ of frequency $f_0 = 1$ kHz $= \omega/2\pi$ and amplitude V_a is applied to the NLCC, where V_a is above the critical reorientation voltage, *Fréedericksz voltage*, $V_{FT} = 6.05$ V$_{pp}$, ranging between 5 and 7 V$_{pp}$. To characterize the Fréedericksz voltage, we have studied the total intensity of the transmitted light as a function of the applied voltage V_a, which shows a supercritical transition (see Fig. 5a). A complementary metal–oxide–semiconductor (CMOS) camera

monitors the NLCC temporal evolution, allowing us to observe the central zone of the magnetic ring. All experimental studies in this setup were conducted at a temperature of 18° C.

This experimental system is described by the same amplitude Eq. (5) [21], but due to the magnet ring, the bifurcation parameter is corrected by a bell-shaped function but with power law decay. In addition, the forcing is also modified by a Rayleigh function with power law decay. We observe a Rayleigh vortex for voltages lower than the molecular reorientation, $V < V_{FT}$, thanks to the microscope illumination system. Fig. 5b shows the vortices observed in the experiment. As the reorientation instability is approached, it is observed that the core structure of the vortex begins to exhibit slight rotation at its center. As the voltage increases, the core of the vortex continues to rotate until it reaches a state of saturation, at which point it ceases to rotate. This phenomenon is illustrated in Fig. 5. Note that from this chart, we show again that the bifurcation is supercritical in nature. Since in this last experiment, the light is used only to illuminate the experiment, it allows better detection of the vortices and their respective transitions (compare Figs. 3 and 5).

The theoretical description for the system under magnetic forcing is analogous to the LCLV system (for more details, see Ref. [21,36]), from the dynamics of the reorientation of $\vec{n}$ described by Eq. (2) adding an external magnetic field $\vec{B}$. The NLCC is also considered to have a homeotropic anchoring and negative electrical and magnetic anisotropy. For a cylindrical magnet, the magnetic field can be modeled in a first approximation by

$$\vec{B}(r,z) = B_r \hat{r} + B_z \hat{z} = m \left[\frac{3zr\hat{r} + (3z^2 - \sigma)\hat{z}}{(r^2 + z^2)^{5/2}} - \frac{l_0^2 \hat{z}}{(r^2 + z^2)^{3/2}} \right] + b_0 \hat{z}, \quad (12)$$

where $\sigma > 0$, l_0, and b_0 are phenomenological dimensional parameters that account for the geometric features of the magnet ring, m is a constant that has a dimension of permeability per magnetic moment, and $\{r, \theta, z\}$ are the cylindrical coordinates. The origin of the coordinate is fixed at the center of the magnetic ring.

By a similar ansatz to (4), close to the reorientation transition, the same Ginzburg–Landau-like amplitude Eq. (5) can be developed, where the bifurcation parameters and the topological forcing must be modified as a function of the external magnetic field [21,36], in the following manner $\mu(r) = -K_3(\pi/d)^2 - \epsilon_a E_z^2 + \chi_a B_r^2(r)$ and $f(r) \equiv -4\chi_a d B_r(r) B_z(r)/\pi a^{1/2}$ where χ_a is the anisotropic magnetic permeability and $a = [(\pi/d)^2(2K_1 - K_3) - 3\epsilon_a E_z^2 - 3\chi_a B_z^2]/4$.

8. Conclusion

We have characterized the formation and transition of different vortex-type solutions in confined and topologically forced liquid crystal cells, which have been used to generate optical vortices. The existence of a Rayleigh vortex centered on a Gaussian beam profile implies that optical vortices are always located at the center of a light beam, which facilitates the generation of optical vortices using light valves or magnetic rings in liquid crystal cells. Our theoretical model, valid close to the reorientation transition, shows qualitative agreement with experimental observations. In addition, the ability to modify the shape of optical vortices provides versatility in the manipulation and generation of optical vortices, opening up new perspectives in image analysis, optical twister, and communications.

The use of liquid crystal light valves, theoretically and experimentally, opens new perspectives on using different light intensity profiles to generate, transition, and stabilize new vortex-like solutions resulting from topological forcing.

CRediT authorship contribution statement

P.J. Aguilera-Rojas: Writing – review & editing, Visualization, Investigation, Data curation. **M.G. Clerc:** Writing – review & editing, Writing – original draft, Validation, Supervision, Resources, Project administration, Methodology, Investigation, Funding acquisition, Formal analysis, Conceptualization. **M. Diaz-Zuniga:** Writing – review & editing, Visualization, Validation, Investigation, Data curation. **R. Gajardo-Pizarro:** Writing – review & editing, Visualization, Investigation, Data curation.

Declaration of competing interest

The authors declare that they have no known competing financial interests or personal relationships that could have appeared to influence the work reported in this paper.

Acknowledgments

Data availability

Data will be made available on request.

References

[1] J.F. Nye, M.V. Nye, Dislocations in wave trains, Proc. R. Soc. Lond. A 336 (1974) 165.

[2] L.M. Pismen, Vortices in Nonlinear Fields, Oxford Science, 1999.

[3] M.S. Soskin, M.V. Vasnetov, in: E. Wolf (Ed.), Progress in Optics, vol. 42, Elsevier, 2001, p. 219.

[4] A.S. Desyatnikov, Y.S. Kivshar, L. Torner, in: E. Wolf (Ed.), Progress in Optics, vol. 47, Elsevier, 2005, p. 291.

[5] L. Allen, M.W. Beijersbergen, R.J.C. Spreeuw, J.P. Woerdman, Orbital angular momentum of light and the transformation of Laguerre-Gaussian laser modes, Phys. Rev. A 45 (1992) 8185.

[6] D.G. Grier, A revolution in optical manipulation, Nature 424 (2003) 810.

[7] V.G. Shvedov, A.V. Rode, Y.V. Izdebskaya, A.S. Desyatnikov, W. Krolikowski, Y.S. Kivshar, Giant optical manipulation, Phys. Rev. Lett. 105 (2010) 118103.

[8] M. Padgett, R. Bowman, Tweezers with a twist, Nat. Photonics 5 (2011) 343.

[9] H.H. Arnaut, G.A. Barbosa, Orbital and intrinsic angular momentum of single photons and entangled pairs of photons generated by parametric down-conversion, Phys. Rev. Lett. 85 (2000) 286.

[10] F. Tamburini, G. Anzolin, G. Umbriaco, A. Bianchini, C. Barbieri, Overcoming the Rayleigh criterion limit with optical vortices, Phys. Rev. Lett. 97 (2006) 163903.

[11] Z.G. Zheng, C.L. Yuan, W. Hu, H.K. Bisoyi, M.J. Tang, Z. Liu, P.Z. Sun, W.Q. Yang, X.Q. Wang, D. Shen, Y. Li, F. Ye, Y.Q. Lu, G. Li, Q. Li, Light-patterned crystallographic direction of a self-organized 3d soft photonic crystal, Adv. Mater. 29 (2017) 1703165.

[12] B.Y. Wei, S. Liu, P. Chen, S.X. Qi, Y. Zhang, W. Hu, Y.Q. Lu, J.L. Zhao, Generation of equal-energy orbital angular momentum beams via photopatterned liquid crystals, Appl. Phys. Lett. 112 (2018) 121101.

[13] J. Wang, J.-Y. Yang, I.M. Fazal, N. Ahmed, Y. Yan, H. Huang, Y. Ren, Y. Yue, S. Dolinar, M. Tur, A.E. Willner, Terabit free-space data transmission employing orbital angular momentum multiplexing, Nat. Photonics 6 (2012) 488.

[14] M.W. Beijersbergen, L. Allen, H.E.L.O. van der Veen, J.P. Woerdman, Astigmatic laser mode converters and transfer of orbital angular momentum, Opt. Commun. 96 (1993) 123.

[15] V.Y. Bazhenov, M.V. Vasnetsov, M.S. Soskin, Laser beams with screw dislocations in their wavefronts, JETP Lett. 52 (1990) 429.

[16] Z. Sacks, D. Rozas, G.A. Swartzlander, Holographic formation of optical-vortex filaments, J. Opt. Soc. Am. B 15 (1998) 2226.

[17] L. Marrucci, C. Manzo, D. Paparo, Optical spin-to-orbital angular momentum conversion in inhomogeneous anisotropic media, Phys. Rev. Lett. 96 (2006) 163905.

[18] E. Brasselet, N. Murazawa, H. Misawa, S. Juodkazis, Optical vortices from liquid crystal droplets, Phys. Rev. Lett. 103 (2009) 103903.

[19] E. Brasselet, Tunable optical vortex arrays from a single nematic topological defect, Phys. Rev. Lett. 108 (2012) 087801.

[20] E. Brasselet, Tunable high-resolution macroscopic SelfEngineered geometric phase optical elements, Phys. Rev. Lett. 121 (2018) 033901.

[21] E. Calisto, M.G. Clerc, V. Zambra, Magnetic field-induced vortex triplet and vortex lattice in a liquid crystal cell, Phys. Rev. Res. 2 (2020) 042026(R).

[22] R. Barboza, U. Bortolozzo, G. Assanto, E. Vidal-Henriquez, M.G. Clerc, S. Residori, Vortex induction via anisotropy stabilized light-matter interaction, Phys. Rev. Lett. 109 (2012) 143901.

[23] R. Barboza, U. Bortolozzo, G. Assanto, E. Vidal-Henriquez, M.G. Clerc, S. Residori, Harnessing optical vortex lattices in nematic liquid crystals, Phys. Rev. Lett. 111 (2013) 093902.

[24] R. Barboza, U. Bortolozzo, M.G. Clerc, S. Residori, E. Vidal-Henriquez, Optical vortex induction via light-matter interaction in liquid-crystal media, Adv. Opt. Photonics 7 (2015) 635.

[25] R. Barboza, U. Bortolozzo, M.G. Clerc, J.D. Davila, M. Kowalczyk, S. Residori, E. Vidal-Henriquez, Light–matter interaction induces a shadow vortex, Phys. Rev. E 93 (2016) 050201(R).

[26] E. Calisto, M.G. Clerc, M. Kowalczyk, P. Smyrnelis, On the origin of the optical vortex lattices in an nematic liquid crystal light valve, Opt. Lett. 44 (2019) 2947.

[27] M.G. Clerc, E. Vidal-Henriquez, J.D. Davila, M. Kowalczyk, Symmetry breaking of nematic umbilical defects through an amplitude equation, Phys. Rev. E 90 (2014) 012507.

[28] P.G. de Gennes, J. Prost, The Physics of Liquid Crystals, second ed., Oxford Science Publications, Clarendon Press, 1993.

[29] S. Chandrasekhar, Liquid Crystals, Cambridge University Press, Cambridge, UK, 1992.

[30] E. Vidal-Henriquez, Phase Singularity Dynamics in Out of Equilibrium Anisotropic Systems (Magister dissertation thesis), University of Chile, https://repositorio.uchile.cl/handle/2250/132990.

[31] S. Kumar, W.B. Cardoso, B.A. Malomed, Stable patterns in the Lugiato–Lefever equation with a confined vortex pump, Symmetry 16 (2024) 470.

[32] L. Pei, D. Huang, W. Fan, H. Cheng, X. Li, Phase-only optically addressable spatial-light modulator and on-line phase-modulation detection system, Appl. Sci. 8 (2018) 1812.

[33] Z. Xing, W. Fan, D. Huang, H. Cheng, T. Du, High laser damage threshold reflective optically addressed liquid crystal light valve based on gallium nitride conductive electrodes, High Power Laser Sci. Eng. 10 (2022) e35.

[34] M.C. Cross, P.C. Hohenberg, Pattern formation outside of equilibrium, Rev. Modern Phys. 65 (1993) 851.

[35] G. Agez, M.G. Clerc, E. Louvergneaux, Universal shape law of stochastic supercritical bifurcations: Theory and experiments, Phys. Rev. E 77 (2008) 026218.

[36] E. Calisto, Vortices Induced By Topological Forcing in Nematic Liquid Crystal Layers (Magister dissertation thesis), University of Chile, https://repositorio.uchile.cl/handle/2250/174821.